Electronic Supplementary Information

Highly Thermoconductive Yet Ultraflexible Polymer Composite with Superior Mechanical Properties and Autonomous Self-Healing Functionality via Binary Fillers Strategy

Dong Wang[1, a], Dingyao Liu[1, b], JianHua Xu[c], JiaJun Fu*[, a] and Kai Wu*[, a, b]

[a] School of Chemistry and Chemical Engineering, Nanjing University of Science and Technology, Nanjing 210094, P. R. China. E-mail: kaiwu@scu.edu.cn; fujiajun668@gmail.com.
[b] College of Polymer Science and Engineering, State Key Laboratory of Polymer Materials and Engineering, Sichuan University, Chengdu 610065, China.
[c] Joint Laboratory of Advanced Biomedical Materials, College of Chemical Engineering, Nanjing Forestry University, Nanjing 210037, P. R. China.
[1] These authors contributed equally to this work.

Experimental Procedures

Results and Discussion

Experimental Procedures

Materials

Hexagonal boron nitride nanosheets (BNNSs), poly (propylene glycol) tolylene, 2,4-diisocyanate terminated (PPGTD, M_n=2300, narrow MW distribution, isocyanate ca. 3.6 wt%), 2,5-dithiobiurea (DTBU, 99%), and isophorone diamine (IDA, 99%) were all purchased from Sigma-Aldrich. Liquid metal (GaInSn, 68.5 wt% Ga, 21.5 wt% In, 10 wt% Sn) was supplied by Flystone Electronics Co. Ltd (Zhejiang Province, China). N, N-Dimethylformamide (DMF) was dried by CaH_2 for 24 h before use. Before fabrication of BNNSs-LM binary fillers, BNNSs were dispersed in water and sonicated for 30 min. The other reagents were of analytical grade and used as supplied without further purification.

Synthesis of PUUE

PPGTD (9.2 g, 4 mmol) was dissolved in 20 mL DMF in a round bottom flask at room temperature and stirred at 0 °C for 10 min under nitrogen atmosphere. The mixture of IDA (0.545 g, 3.2 mmol) and DTBU (0.12 g, 0.8 mmol) in DMF (12 mL) was cooled to 0 °C and slowly added into the round bottom flask under vigorous stirring within 10 min. The reaction mixture was stirred for 12 h at 0 °C and then heated to 85 °C for another 12 h stirring under nitrogen atmosphere. After that, the product was poured into a polytetrafluorethylene (PTFE) mold and dried at 90 °C for 48 h in an air-circulating oven, followed by drying at 75 °C in vacuum oven for 12 h to remove residual solvent and bubbles. The PUUE specimen was finally peeled off from the PTEE mold for further use.

Fabrication of BNNSs$_{27}$-LM$_{27}$/PUUEC

The BNNSs-LM binary fillers are prepared by intense physical mixing for 30 minutes using high-speed disperser (Ultra-Turrax UTC, IKA) to ensure the maximal interaction between BNNSs and LM. The weight fractions of BNNSs and LM are equal in binary fillers. The fabrication of BNNSs$_{27}$-LM$_{27}$/PUUEC was as following: Firstly, 10 g PUUE was dissolved in 11.54 g DMF under magnetic stirring at 60 °C for 4 hours. Then the solution was mixed with 12 g BNNSs-LM binary fillers through shear induced turbulent for 10 minutes until obtaining a homogeneous viscous composite solution. Afterwards, the composite solution was co-precipitated in deionized water. The collected precipitates were dried in vacuum oven to remove residual solvent at 75 °C for 48 hours. The as-prepared composite was processed into desired shape by hot-pressing at 60 °C. By controlling binary fillers loading, a series of BNNSs$_x$-LM$_x$/PUUECs (x=8, 14, 22, 27, and 31) were prepared. The same procedure was used to prepare BNNSs$_{27}$/PUUEC (3.75 g BNNSs instead of binary fillers), LM$_{27}$/PUUEC (3.75 g LM instead of binary fillers) and BNNSs$_{54}$/PUUEC (12 g BNNSs instead of binary fillers).

Characterizations

^{1}H NMR spectrum was recorded on a Bruker AVANCE III 500 MHz NMR spectrometer at room temperature using the deuterated solvent and TMS as the internal reference. FTIR spectra were recorded using a Bruker Tensor 27 Fourier transform infrared spectrometer equipped with a Specac Golden Gate MK II ATR heating cell in the range between 4000-600 cm^{-1} with a resolution of 4 cm^{-1}. The temperature-dependent FTIR data were selected to proceed 2D correlation analysis. The software 2D Shige version 1.3 was used to deal with raw data in the predetermined wavelength ranges. In the two-dimensional correlation FTIR spectroscopy, the red and blue colors represent the positive and negative correlation intensities, respectively. The crystal phase of the poly(urea-urethane) elastomer was analyzed via XRD (Bruker D8 Advance) using monochromatized Cu Kα radiation (λ=0.1541 nm). X-ray photoelectron spectroscopy (XPS) was carried out by using an Axis Ultra DLD (UK). TGA was performed using a Mettler 851e instrument with the heating rate of 10 °C min^{-1} from 50 to 500 °C in nitrogen flow. DSC experiments were carried out on a TA DSC-25 instrument at a heating rate of 10 °C min^{-1} under nitrogen atmosphere. The surface morphologies of BNNSs were observed using AFM (Bruker Multimode 8) in the tapping mode. STEM-EDS spectra were recorded from an FEI-Tecnai G2 F30 S-TWIN TEM instrument operated at 200 kV. The digital photographs were gathered by a Canon EOS 80D. The electrical conductivity was measured by a Keithley 2450 SourceMeter. The temperature distribution images were recorded by an FLIR A615 infrared thermograph and the ambient temperature was appropriately 25 °C. In-plane thermal conductivity and out-of-plane thermal conductivity of polymer and polymer composites were calculated according to the equation $k = \rho \times C \times D$, where k, ρ, C, and D correspond to thermal conductivity (W m^{-1} K^{-1}), density (g cm^{-3}), specific heat capacity (J g^{-1} K^{-1}), and thermal diffusivity (mm^2 s^{-1}). The thermal diffusivities of the specimens were measured by TA DXF-900 instrument, where the voltage and tested temperature were set to be 500-550V and 25 °C, respectively. The densities of the specimens were tested using an automatic density analyzer (UltraPYC 1200e, Quantachrome Instruments) at room temperature in atmosphere of helium. Specific heat capacities of the specimens were evaluated by a TA DSC-25 instrument using sapphire mode.

Mechanical testing

Mechanic strain-stress experiments were performed using a Shimadzu AGS-X tester. The size of polymer/polymer composite specimens is 30 mm (length) × 10 mm (width) × 1.0 mm (thickness). A strain rate and a gauge length were controlled as 100 mm min^{-1} and 5 mm, respectively. All specimens were tested at ambient conditions (25 °C, RH=55%). In the cyclic tensile test, stretching and retracting processes were also tested at a strain rate of 100 mm min^{-1}. The dynamic mechanical properties of polymer/polymer composites were performed using a TA DMA Q800 instrument. For

temperature sweep experiments, the specimens (5 mm × 5 mm × 0.5 mm) were first cooled to -60 °C and then followed to a heating scan at 5 °C min^{-1} to 50 °C under nitrogen atmosphere with a frequency of 1 Hz. For stress-relaxation experiments, the specimens were stretched to 100% and maintained, the time-dependent relaxation responses of stress were recorded. Dimensions of the specimens for DMA measurements were determined by a standard vernier calliper. Bulk rheological experiments were tested on TA AR-G2 rheometer using 20 mm parallel plate attachment. Frequency sweeps were tested at a strain amplitude of 0.5% by varying the frequency between 100 rad/s to 0.1 rad/s in the temperature range of 25-80 °C.

Results and Discussion
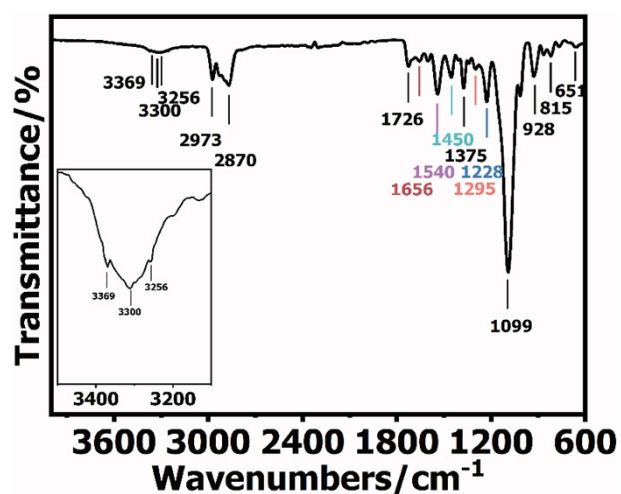
Fig. S1 FTIR spectrum of PUUE. FTIR (cm^{-1}): 3256 (v_{-NH-},thiourea), 3300 (v_{-NH-}, urea), 3369 (v_{-NH-}, carbamate), 2870/2973 (v_{-CH3}), 1375 (δ_{-CH3}), 1656 ($v_{C=O}$, urea), 1726 ($v_{C=O}$, urethane), 1450 ($v_{C=S}$),928/651 (δ_{-C7H6-}) and 1540 (v_{-NH-}),1228 ($v_{(-C-C-)s}$), and 1099 ($v_{-C-O-C-}$).
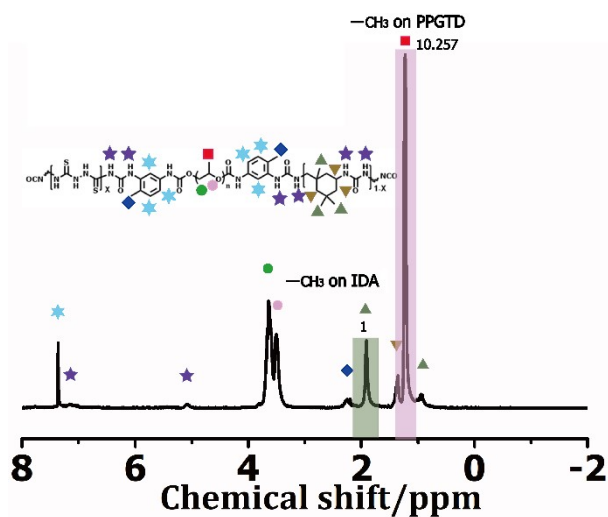
Fig. S2 ^{1}H NMR spectrum of PUUE (300 MHz, CDCl3, room temperature). As shown in Figure S2, based on the ^{1}H NMR analysis, the poly(urea-urethane) elastomer with a feed monomer molar ratio of PPGTD:IDA:DUTB being 1:0.8:0.2 have the measured monomer molar ratio of 1:0.78:0.22.
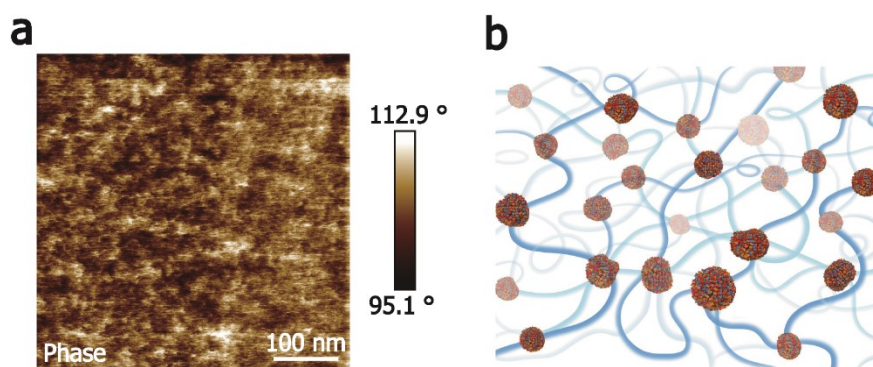
Fig. S3 a) AFM image of PUUE. b) Schematic illustration of chemical structure of PUUE. AFM phase image provides an obvious evidence of a microphase-separated structure, where hierarchical H-bonds assemble hard phase, and poly(propylene glycol) chains act as soft phase, is clearly depicted in Figure S3b.

M_n:46600
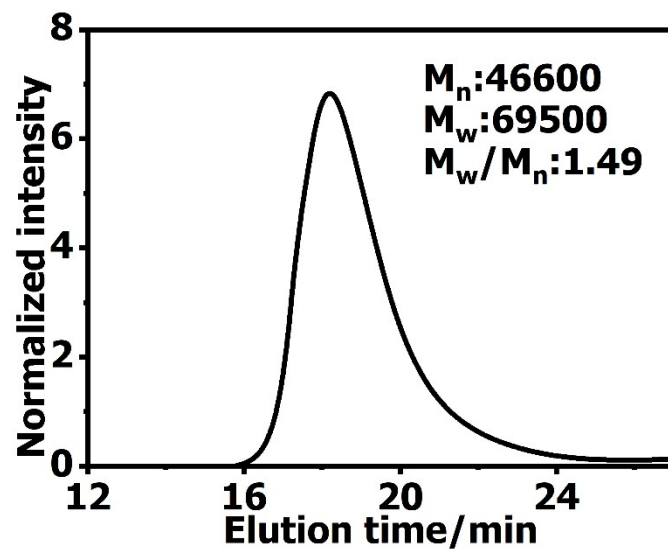M_w:69500
M_w/M_n:1.49

Figure S4 GPC elution curve of PUUE with DMF as the eluent and PMMA as standard.
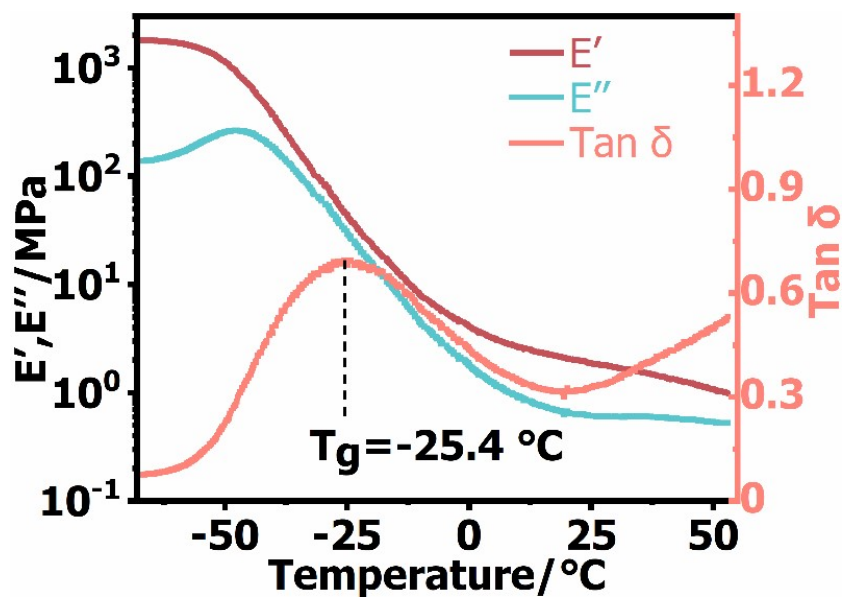
Fig. S5 Temperature dependency of the storage modulus (E'), loss modulus (E''), and loss factor (tan δ) of PUUE. As shown in tan δ curve, the glass-transition temperature (T_g) is about -25.4 °C.
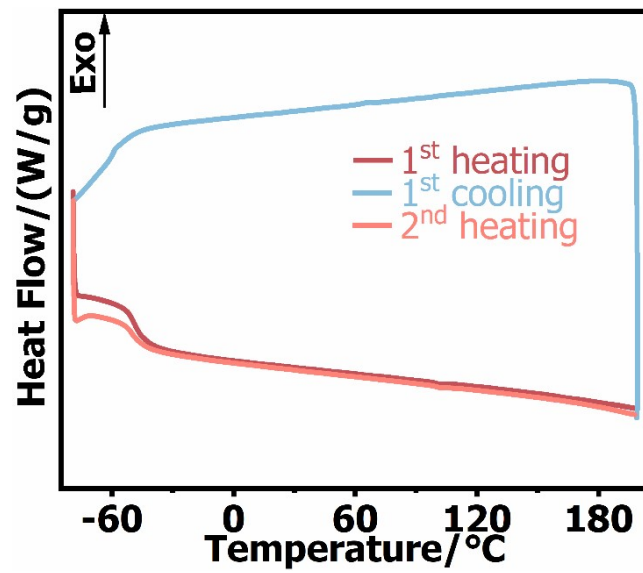
Fig. S6 DSC curves of PUUE.
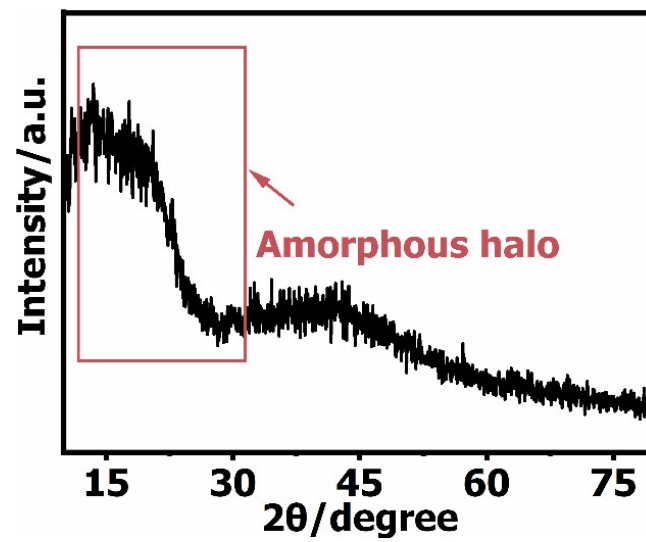
Fig. S7 XRD curve of PUUE. As shown, the XRD curve of PUUE only displayed a broad diffraction peak centered at 2ϑ=14.2°. The lack of crystalline peaks found in XRD data prove that PUUE is amorphous.

Table S1. The parameters of mechanical properties for PUUE.

Sample	Elongation at break(%)	Young's modulus(Mpa)	Tensile strength(Mpa)	Toughness (MJ m^{-3})
PUUE	4520	0.66	0.99	37.96

Fig. S8 Anti-puncture perfromance of PUUE.

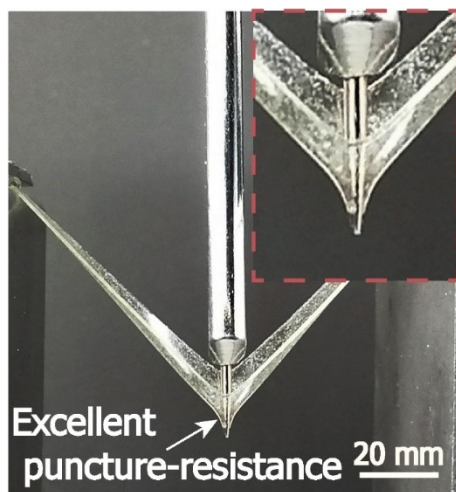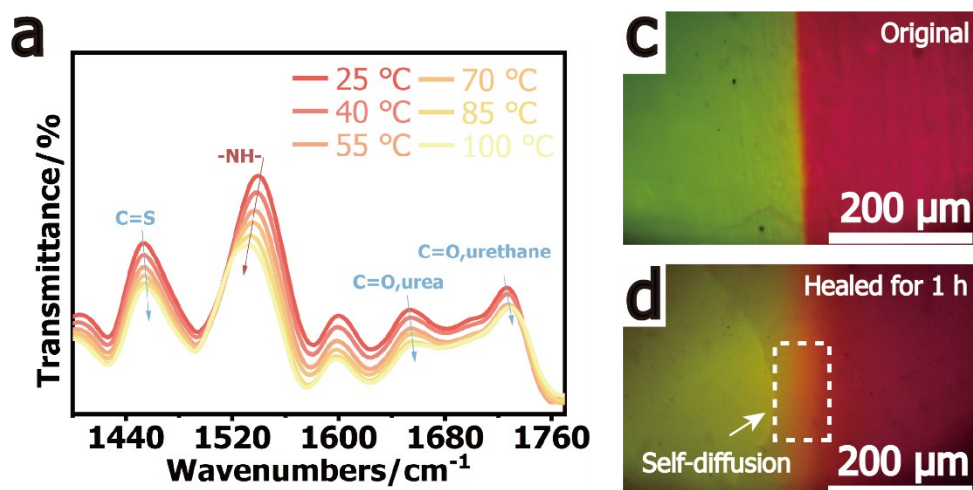**Figure S9** (a) The temperature-dependent FTIR spectra of PUUE from 25 °C to 100 °C with an increment of 15 °C in the wavelength range of 1400-1770 cm^{-1}. With the increase of temperature, the peaks of υ (C=S), υ (C=O$_{Urea}$) and υ (C=O$_{Urethane}$) all showed a blueshift and υ (-NH-) showed a redsheft. (b) Comparisons of fluorescence micro-scopic images before and after healed. Two separated blocks were stained by rhodamine B and FITC, respectively. The appearance of fusion area formed for the overlap of red rhodamine B and fluorescein revealed the diffusion of polymeric chains of PUUE.
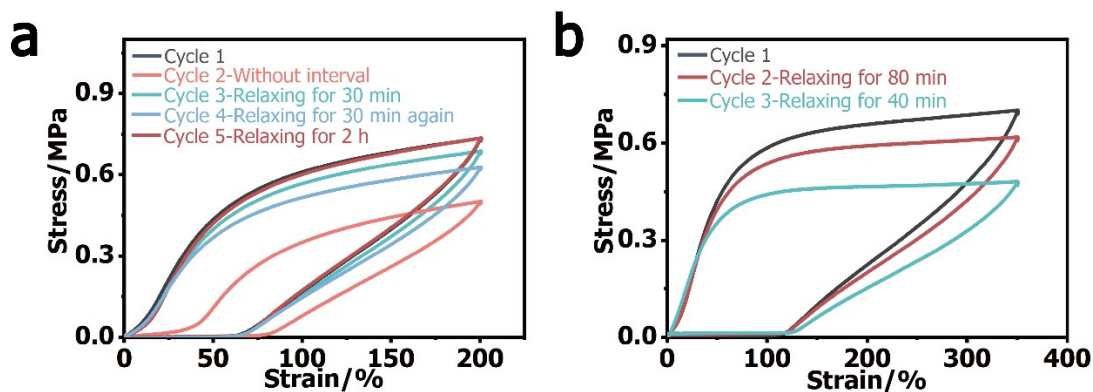
Figure S10 Cyclic tensile curves of PUUE at a loading/unloading rate of 100 mm min^{-1} at 25 °C. (a) The specimen was loaded to 200% and immediately reloaded. Then, the specimen was allowed to relax for 30 min and 2 h at room temperature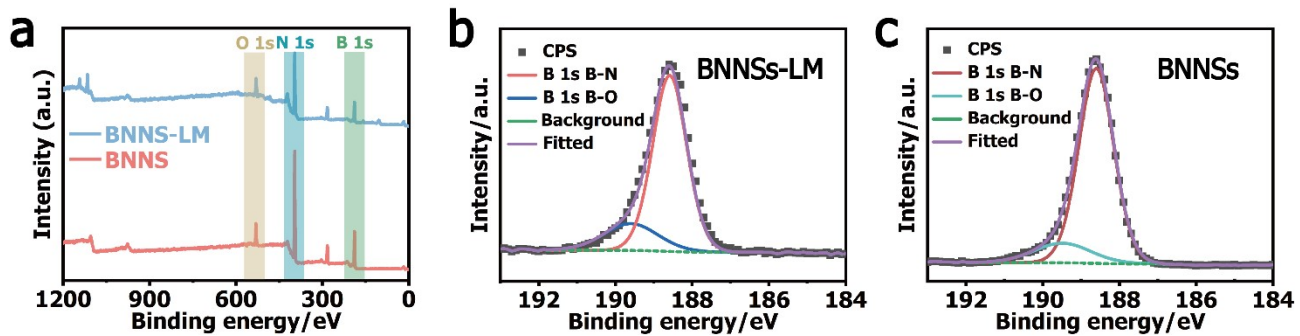 to eliminate residual strain and recovery hysteresis loop, respectively. (b) Cyclic tensile curves of PUUE at 350% strain at the time interval of 40 min and 80 min. As depicted in **Fig. S10a**, the deformation was quickly recovered within 30 min, and elasticity could recover completely within 2 h. What's more, the PUUE illustrated a full tensile deformation recovery for strains to 350% after a 40 min resting period (**Fig. S10b**). The elasticity and recoverable energy dissipation capacity are attributed to the relatively fast reformation of dynamic networks crosslinked by the dynamic hierarchical H-bonds.

Table S2. The parameters of mechanical properties and healing efficiencies for PUUE during different healing time.

Healing time	Toughness (MJ/m^3)	Elongation at break(%)	Tensile strength(Mpa)	Healing efficiency(%)
Original	37.96	4529	0.99	/
3 h	11.02	1962	0.71	29.03
6 h	23.44	3259	0.91	61.75
12 h	33.96	4143	1.01	89.47
24 h	37.61	4520	1.02	99.09

Fig. S11 XPS characterization of BNNSs-LM binary fillers. a) XPS wide spectrum of BNNSs and BNNSs-LM binary fillers. b) B1s core level of BNNSs. c) B1s core level of BNNSs-LM binary fillers.
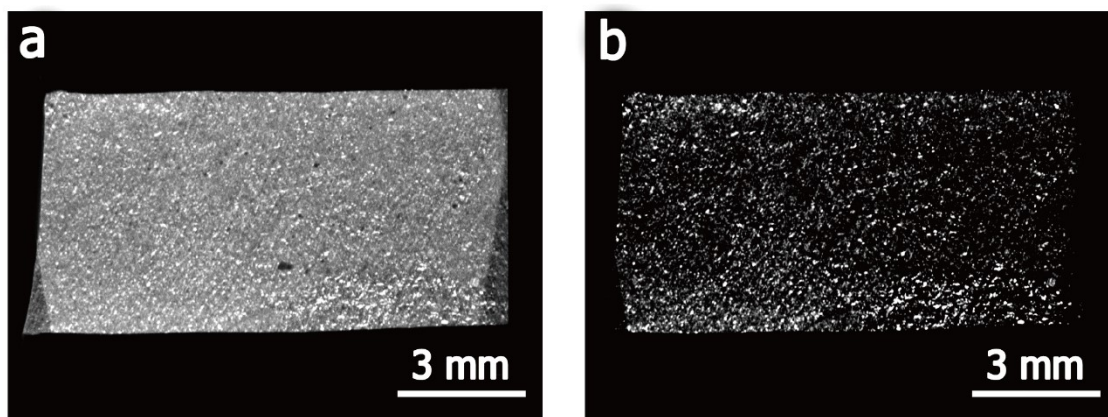
Fig. S12 a) Micro computed tomography of BNNSs$_{27}$-LM$_{27}$/PUUEC. b) Micro computed tomography of BNNSs$_{27}$-LM$_{27}$/PUUEC showing the distribution of both BNNSs and LM at the normal state while eliminating the signal of PUUE matrix. Noted that the X-ray attenuation of LM and BNNSs is much significant than PUUE matrix due to their large difference in density. Therefore, adjusting the testing parameters, the distribution of LM and BNNSs could be given through further processing.
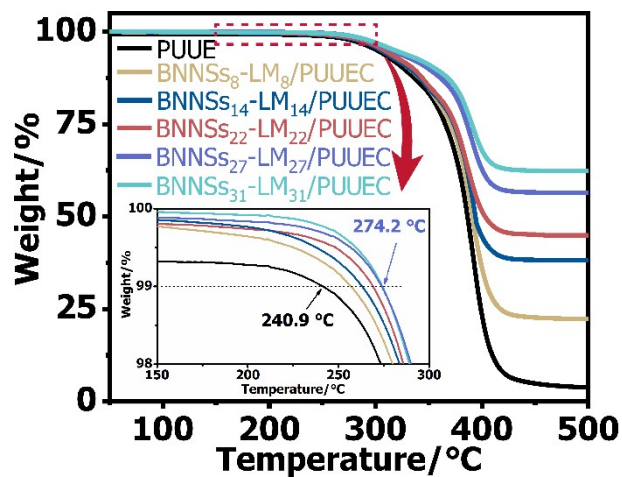
Fig. S13 TGA curves of BNNSs$_x$-LM$_x$/PUUECs (x=8, 14, 22, 27, and 31) upon heating from 50 to 500 °C at a rate of 10 min^{-1}. Inset demonstrating that with the increase in loading mass of BNNSs-LM binary fillers, the onset degradation temperature gradually increased.

Table S3. The parameters of mechanical properties for BNNSs$_x$-LM$_x$/PUUECs.

Sample	Elongation at break(%)	Young's modulus(Mpa)	Tensile strength(Mpa)	Toughness (MJ m^{-3})
PUUE	4520	0.61	0.99	37.96
BNNSs$_8$-LM$_8$/PUUEC	4190	0.84	1.61	57.17
BNNSs$_{14}$-LM$_{14}$/PUUEC	3880	1.42	1.81	60.46
BNNSs$_{22}$-LM$_{22}$/PUUEC	3630	2.15	2.63	89.26
BNNSs$_{27}$-LM$_{27}$/PUUEC	3485	2.97	3.10	99.92
BNNSs$_{31}$-LM$_{31}$/PUUEC	1600	7.20	5.03	71.30

Elongation at break(%)	Young's modulus (Mpa)	Tensile strength (Mpa)	Toughness (MJ m^{-3})
1374	6.98	5.23	65.03
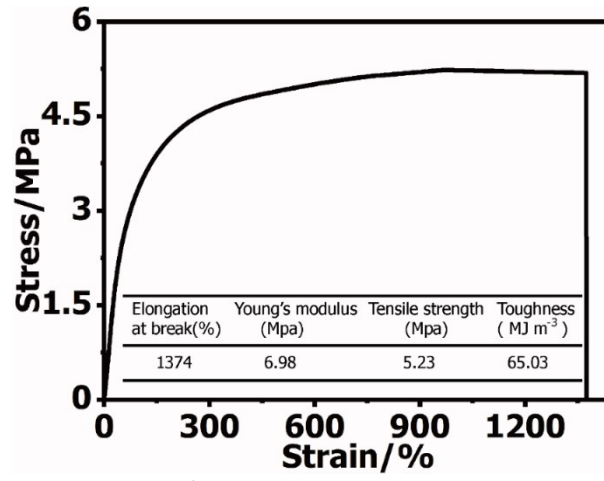
Fig. S14 Tensile stress-strain curve of the BNNSs$_{27}$/PUUEC. Inset showing the parameters of mechanical properties.
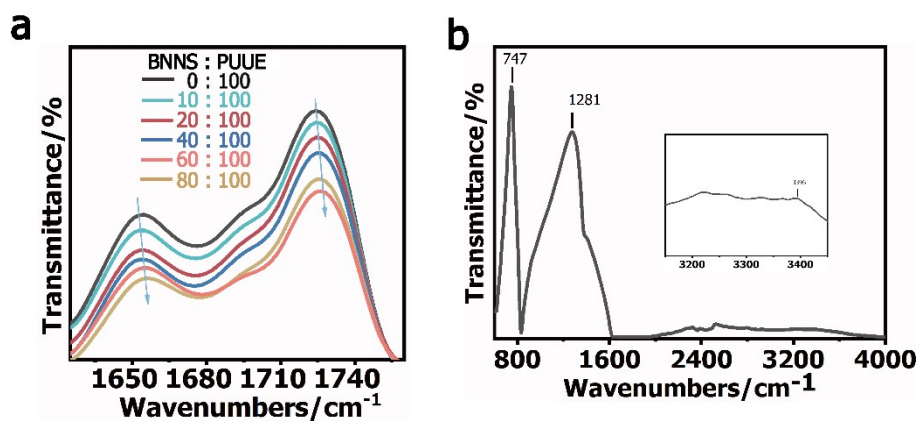
Fig. S15 a) FTIR spectra of BNNSs/PUUECs with different weight fraction of BNNSs. b) FTIR spectrum of BNNSs. 747 cm^{-1} (v_{B-N}), 1281 cm^{-1}(δ_{B-N}), 3396 cm^{-1} (v_{-OH}). As shown in Figure S15a, with the increase in weight fraction of BNNSs, the two stretching vibration bands of C=O at 1726 cm^{-1} (carbamate unit) and 1656 cm^{-1} (urea unit) all exhibited blueshift, accompanied by the reduction of intensity. These phenomena indicate the formation of interfacial H-bonds between BNNSs-OH and PUUE.
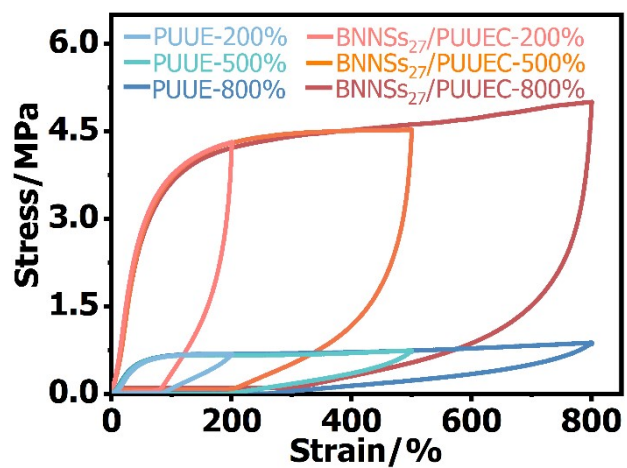
Fig. S16 Loading-unloading tensile tests for BNNSs$_{27}$/PUUEC and PUUE at the strains of 200%, 500%, and 800%. As shown in Figure S13, the hysteresis loop of BNNSs$_{27}$/PUUEC was much higher than that of PUUE at each strain, confirming that the interfacial noncovalent bonds were ruptured to dissipate energy.
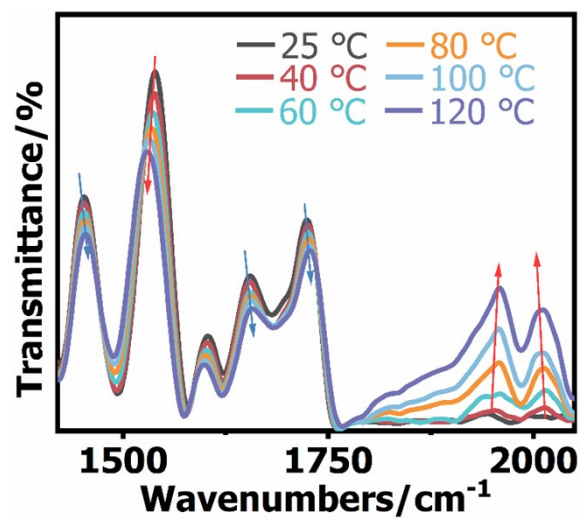
Fig. S17 Temperature-dependent FTIR spectra of LM$_{27}$/PUUEC in the temperature range from 25 °C to 120 °C. The reversible shifts demonstrates the dynamic nature of interfacial metal-ligand interactions.
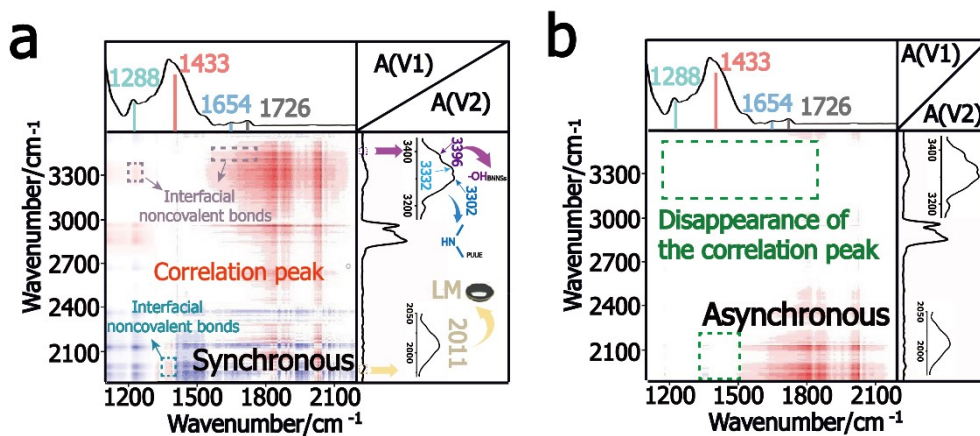
Fig. S18 a) Synchronous and b) asynchronous two dimensional correlation FTIR spectra of BNNSs$_{27}$-LM$_{27}$/PUUEC.
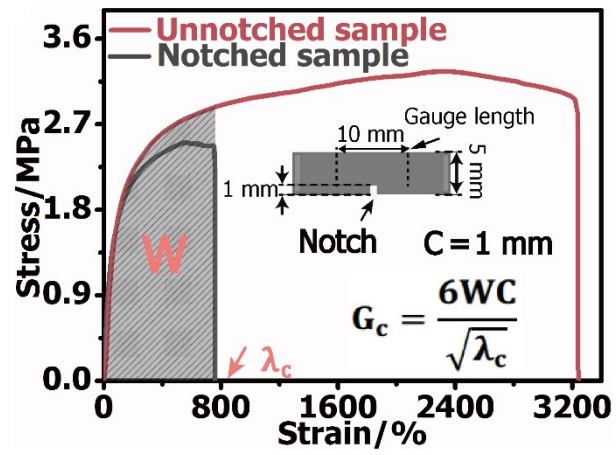
Fig. S19 Stress-strain curves of the notched and unnotched $BNNSs_{27}$-LM_{27}/PUUEC. A 1 mm notch was artificially made on a 5 mm wide rectangular specimen. Inset showing the Greensmith calculation method for fracture toughness.
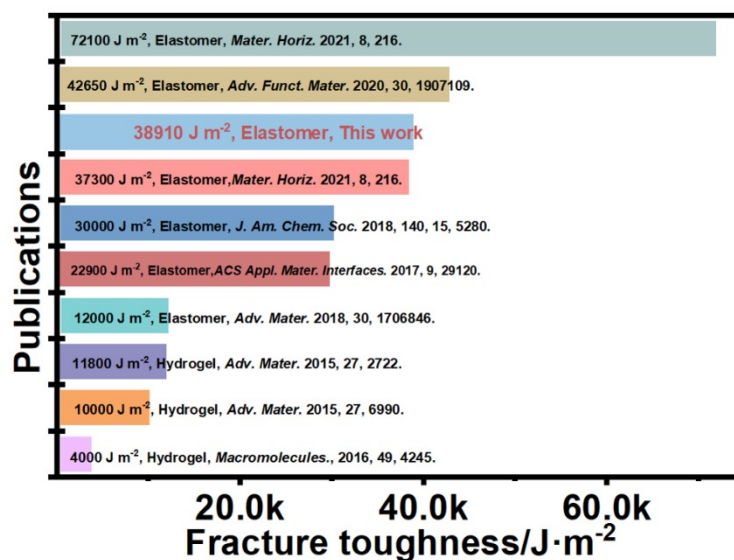
Fig. S20 Comparisons of fracture toughness. Fracture toughness of BNNSs$_{27}$-LM$_{27}$/PUUEC and the other recently reported room-temperature self-healing polymers with relatively high fracture toughness.
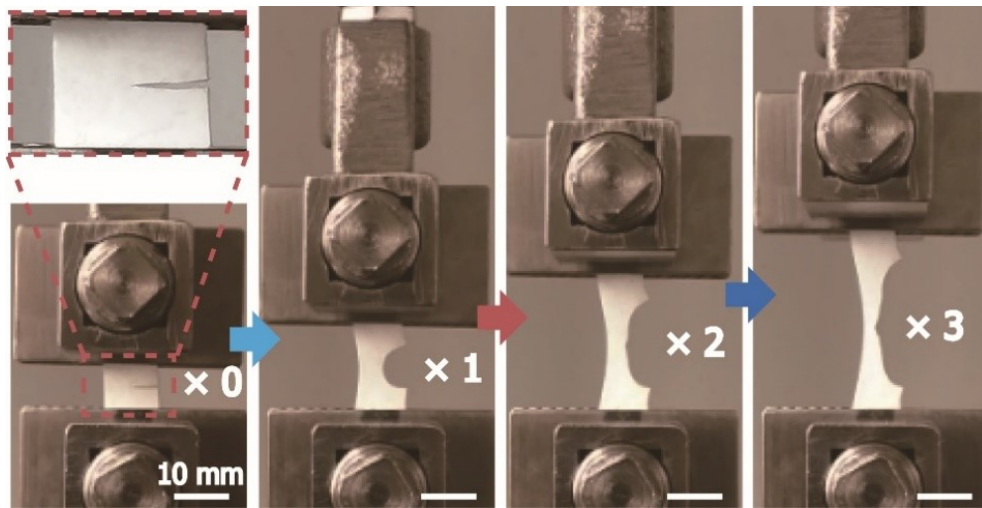
Fig. S21 Photographs for the stretching process of the notched BNNSs$_{27}$/PUUEC specimen. As shown in Figure S21, BNNSs$_{27}$/PUUEC specimen was stretched to more 3-folds its original length with an artificial notch (6 mm, half of width of the specimen), which is far inferior to BNNSs$_{27}$-LM$_{27}$/PUUEC.

Table S4. The parameters of mechanical properties and healing efficiencies for BNNSs$_{27}$-LM$_{27}$/PUUE during different healing time.

Healing time	Toughness (MJ/m^3)	Elongation at break(%)	Tensile strength(Mpa)	Healing efficiency(%)
Original	99.92	3485	3.11	/
6 h	28.36	1214	2.78	28.39
12 h	58.91	2179	2.93	58.96
24 h	83.75	3001	3.03	83.81
40 h	98.26	3459	3.12	98.34
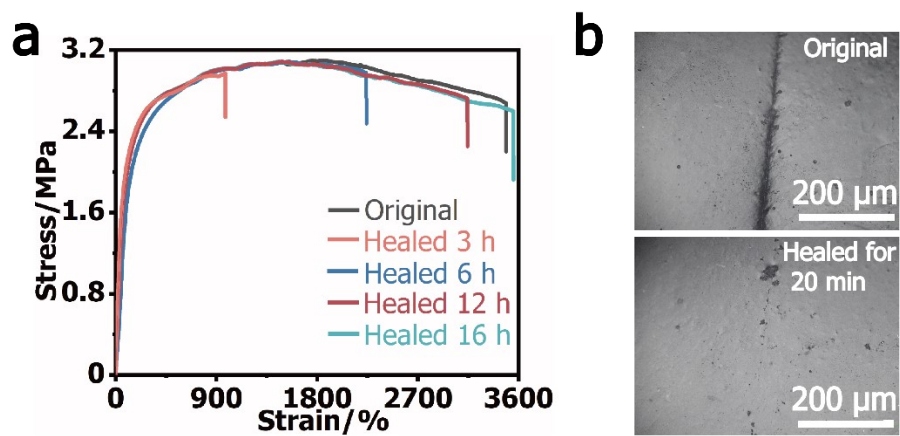
Fig. S22 (a) Tensile stress-strain curves of BNNSs$_{27}$-LM$_{27}$/PUUEC at different healing times under 60 °C. (b) Optical microscopy images of BNNSs$_{27}$-LM$_{27}$/PUUEC with an artificial scratch before and after healed under 60 °C.

Table S5. The mechanical properties and healing efficiencies parameters for BNNSs$_{27}$-LM$_{27}$/PUUE during different healing times under 60 °C.

Healed time	Toughness (MJ/m^3)	Elongation at break(%)	Healing efficiency(%)
Original	99.92	3485	/
Healed 3 h	25.65	984	25.67
Healed 6 h	62.91	2240	62.96
Healed 12 h	89.61	3143	89.68
Healed 16 h	100.43	3554	100

Fig. S23 Tensile stress-strain curves of BNNSs$_{27}$/PUUEC at different healing time under ambient condition.

Table S6. The mechanical properties and healing efficiencies parameters for $BNNSs_{27}$/PUUE during different healing times under ambient conditions.

Healed time	Toughness (MJ/m^3)	Elongation at break(%)	Healing efficiency(%)
Original	65.03	1374	100
Healed 6 h	14.29	388	28.24
Healed 12 h	15.99	432	31.44
Healed 24 h	22.65	575	41.85
Healed 40 h	32.46	775	56.40
Healed 52 h	36.84	853	62.08

Fig. S24 Temperature dependency of the loss factor (tanδ) of PUUE, BNNSs$_{27}$/PUUEC, BNNSs$_{27}$-LM$_{27}$/PUUEC and LM$_{27}$/PUUEC at a scan rate of 5 °C min^{-1}.

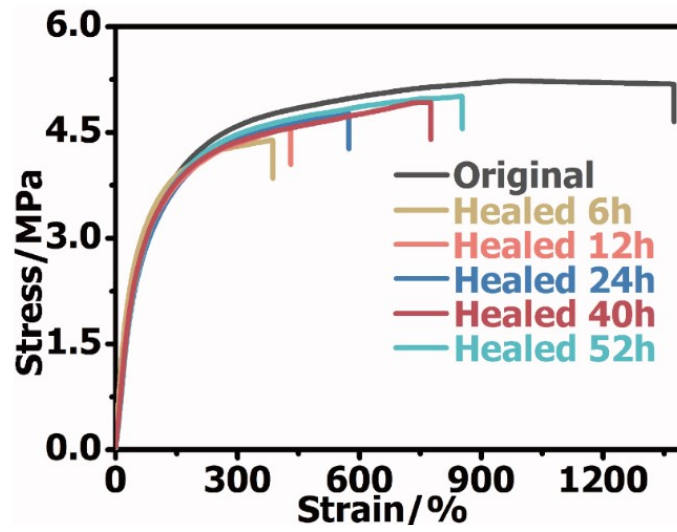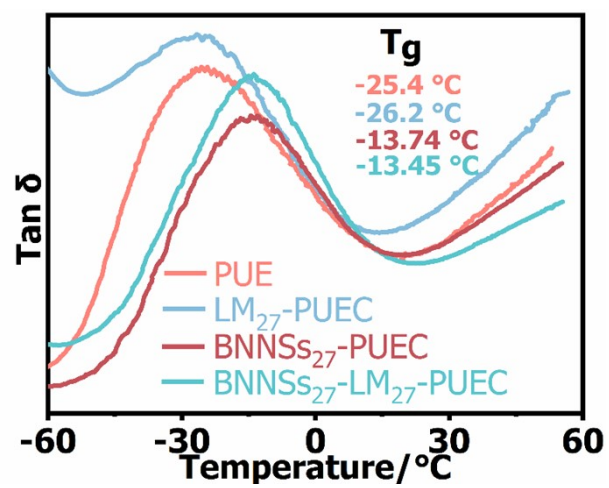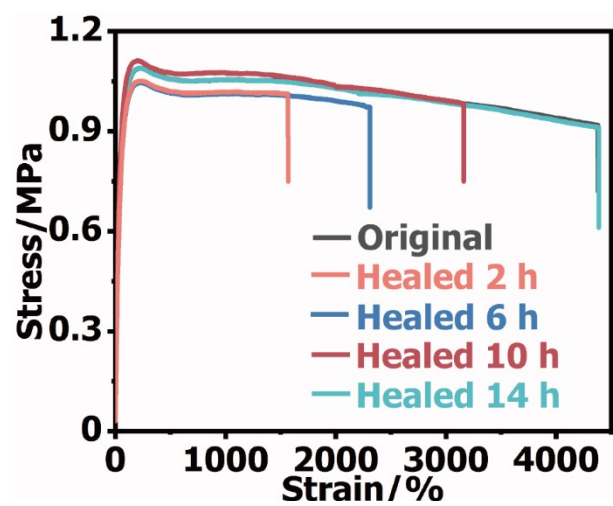**Fig. S25** The tensile stress-strain curves of LM$_{27}$/PUUEC at different healing time under ambient condition.

Table S7. The mechanical properties and healing efficiencies parameters for LM_{27}/PUUE during different healing times under room temperature.

Healed time	Toughness (MJ/m^3)	Elongation at break(%)	Healing efficiency(%)
Original	44.03	4378	/
Healed 2 h	15.66	1568	35.57
Healed 6 h	22.95	2316	52.12
Healed 10 h	32.87	3163	74.65
Healed 14 h	43.97	4386	99.86
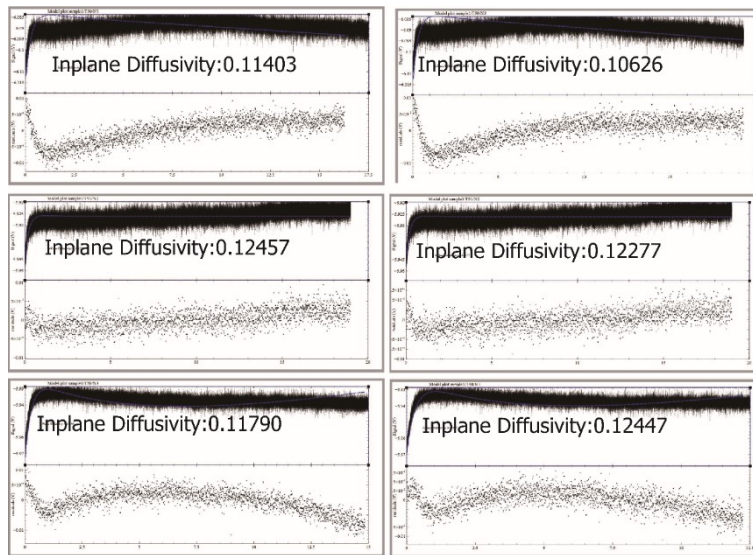
Fig. S26 Proofs for thermal conductivity of BNNSs$_{27}$-LM$_{27}$/PUUEC at the thickness of 85 μm. Six photographs showing the tested and fitted curves about in-plane thermal diffusivity (cm^2 s^{-1}) of BNNSs$_{27}$-LM$_{27}$/PUUEC specimens. The density and the specific heat capacity of BNNSs$_{27}$-LM$_{27}$/PUUEC are 1.68 g cm^{-3} and 1.34 J g^{-1} K^{-1}, respectively.
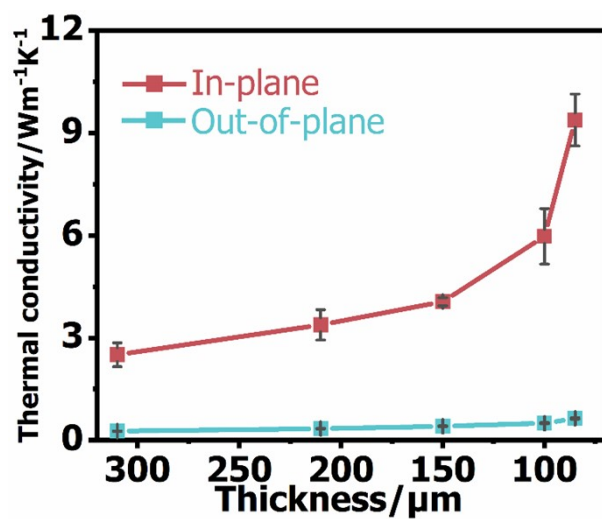
Fig. S27 In-plane and out-of-plane thermal conductivity of BNNSs$_{27}$/PUUEC specimen at various thickness. The density and the specific heat capacity of BNNSs$_{27}$/PUUEC are 1.13 g cm^{-3} and 1.81 J g^{-1} K^{-1}, respectively.
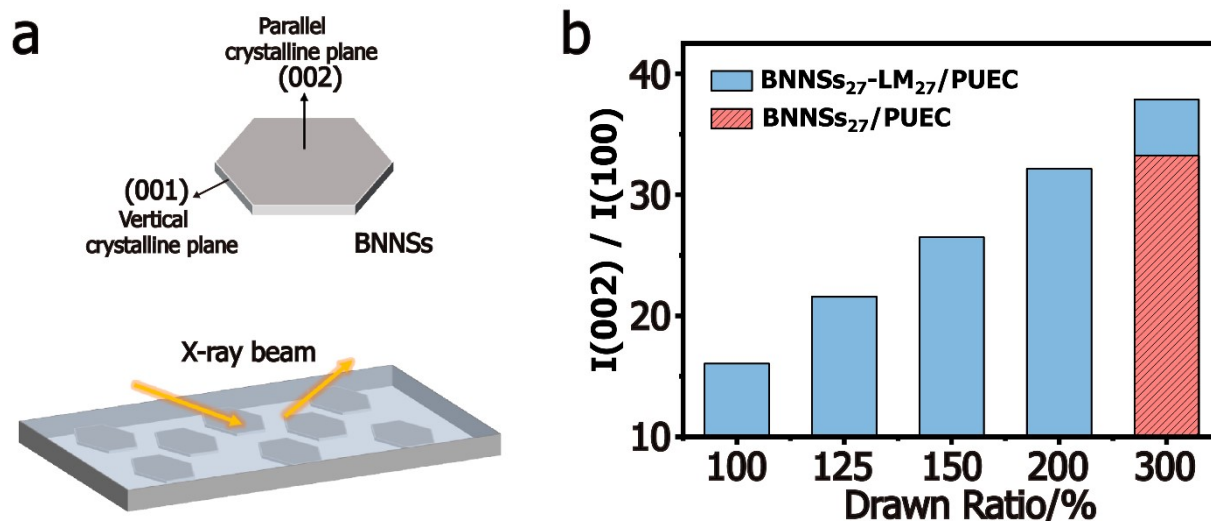
Fig. S28 a) Schematic diagram of the crystal plane for BNNSs (up) and XRD characterization of specimen (down), the orientation of BNNSs along in-plane direction could be reflected from the ratio of the intensity between peak (002) and (100). b) The intensity ratio between peak of (002) and peak of (100) with the increase of strain.

The orientation of fillers, including BNNSs-LM and BNNSs, was characterized by XRD patterning. The (100) and (002) peaks respectively correspond to the vertical and parallel crystalline planes of BNNSs, and the orientation degree of BNNSs along in-plane direction can be reflected from the ratio between the intensity (I) of peak (002) and (100) (Figure S28a). Specifically, the larger the ratio is, the better the in-plane orientation of BNNSs is. To verify the orientation of the polymer composite, the specimen was tested by hitting the X-ray beam onto the upper surface. As learned from Figure S28b, an obvious increase of I(002)/I(100) was found (from 16.2 to 36.8) with the increase of drawn ratio, confirming that the uniaxial stretching can facilitate BNNSs to be oriented along in-plane direction.
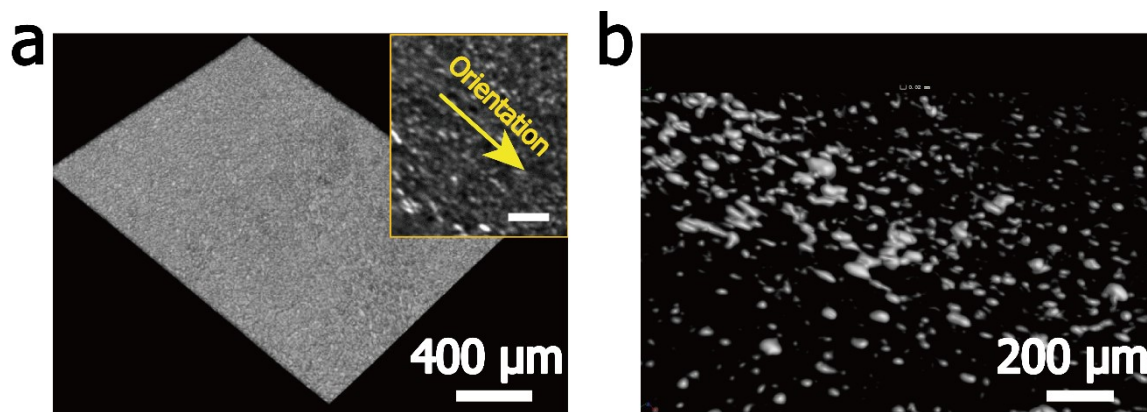
Fig. S29. a) Micro computed tomography of stretched BNNSs$_{27}$-LM$_{27}$/PUUEC. b) Micro computed tomography of the morphology and distribution of LM droplets at the deformed state. Noted that the signals of polymer matrix and BNNSs are eliminated.

Micro computed tomography is a non-destructive technique that has been widely applied to visualize the internal geometry and distribution of fillers within composite materials. The micro computed tomography scan can present good contrast images as long as there is a significant difference in X-ray attenuation within heter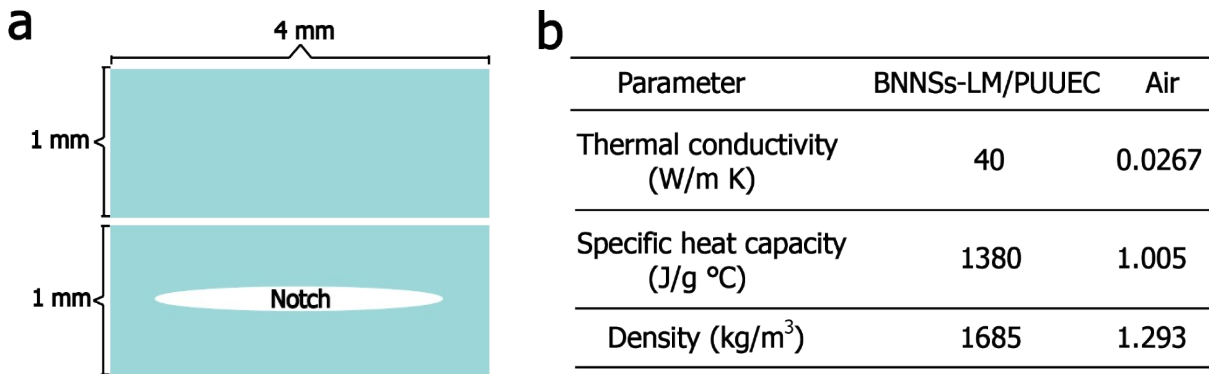ogeneous systems. Herein, the morphology of deformed BNNSs$_{27}$-LM$_{27}$/PUUEC was studied through image of original micro computed tomography, as shown in Figure S29a, the inset image gives clear vision that BNNSs-LM binary fillers are oriented along the deformed direction. It should be noted that the X-ray attenuation of LM is much significant than PUUE matrix and BNNSs due to their large difference in density. Therefore, the distribution of LM could be given through further processing. As shown in Figure S29b, the obvious deformation of LM droplets could be observed at the deformed state, which is beneficial for bridging adjacent BNNSs-LM within the composite. Meanwhile, it was found that LM droplets do not form percolative network through the whole sample in such filler content, which is a good explanation for the insulation properties of the polymer composite.
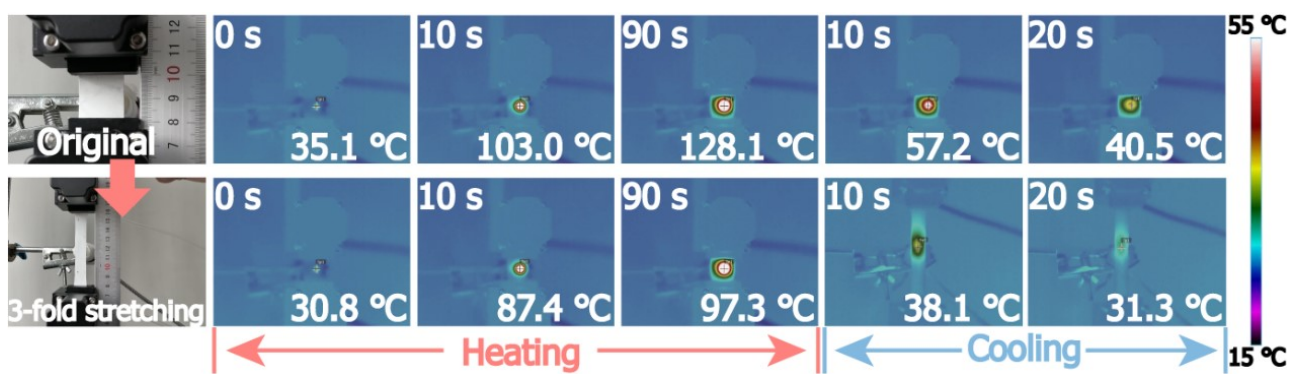
Fig. S30 Photographs of BNNSs$_{27}$/PUUEC under normal and stretched (300%) states. Infrared thermal images of BNNSs$_{27}$/PUUEC irradiated by NIR at different time (including heating and cooling stages).

a

4 mm

1 mm

1 mm

Notch

b

| Parameter	BNNSs-LM/PUUEC	Air
Thermal conductivity (W/m K)	40	0.0267
Specific heat capacity (J/g °C)	1380	1.005
Density (kg/m^3)	1685	1.293

**Fig. S31** a) The model and b) parameters used in finite elemen simulation.

Finite element analysis was used to simulate the impact of notches on heat dissipation. The models for original and notched polymer composite are constructed and shown in Figure S31a-b. Herein, a parallel heat source (85 °C) was applied on the top of the specimen, and the heat sink (on the bottom) was set with a constant temperature of 25 °C to ensure the heat flow from the top to the bottom of the specimen. During the heat dissipation process, the temperature and distribution of heat flux vector within composite are simulated based on classical Flourier Law, $q=-k\times$grad(T), where q is the heat flux, k is the thermal conductivity, and grad(T) is the temperature gradient. The calculative distribution of temperature is visualized in Figure 6d(i), which clearly shows that the heat is mainly concentrated in area between the notch and the heat source, and the heat cannot be effectively transferred to the other side. Heat flux is a parameter that reflects the intensity of heat dissipation with its arrow leads to the direction of heat flow. As shown in Figure 6d(ii), it was found the notch greatly impedes the heat flux transporting from the heat source to sink, and most heat flux is concentrated around the edge of the notch, further signifying the negative influence of notch on heat dissipation.
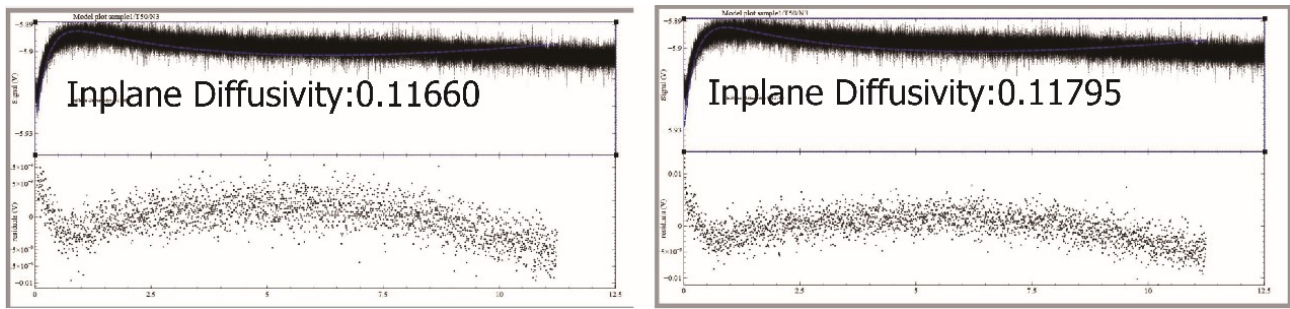
Fig. S32 The tested and fitted curves about in-plane thermal diffusivity ($cm^2\ s^{-1}$) of BNNSs$_{27}$-LM$_{27}$/PUUEC specimen (left side), and BNNSs$_{27}$-LM$_{27}$/PUUEC specimen was artificially scratched and healed for 2 h (right side). As shown in Figure S29, the thermal diffusivity of BNNSs$_{27}$-LM$_{27}$/PUUEC remained stable after healing for 2 h, indicating the restoration of thermally conductive path via intrinsic self-healing mechanism.
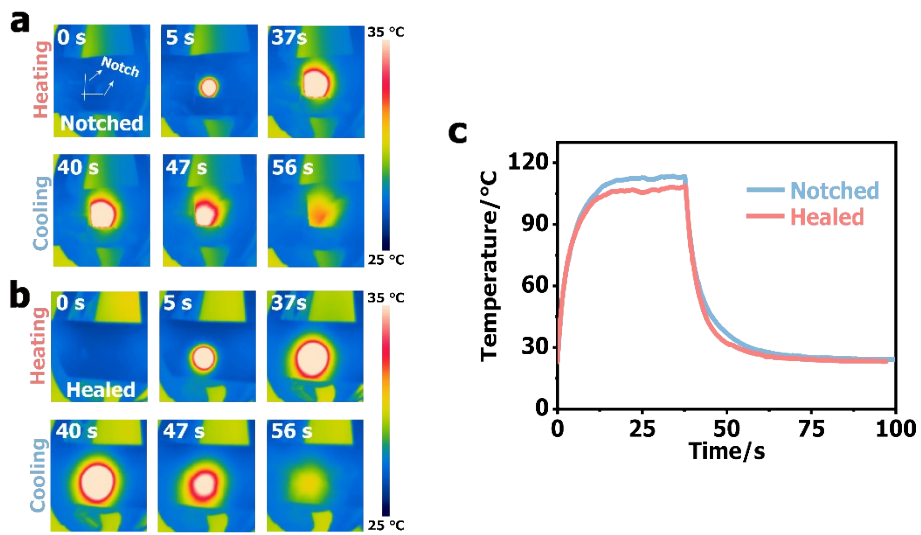
Fig. S33 a) IR images of notched BNNSs$_{27}$-LM$_{27}$/PUUEC and b) healed BNNSs$_{27}$-LM$_{27}$/PUUEC when being heated by an infrared laser transmitter. c) Maximum temperature versus time curves of notched and healed BNNSs$_{27}$-LM$_{27}$/PUUEC.
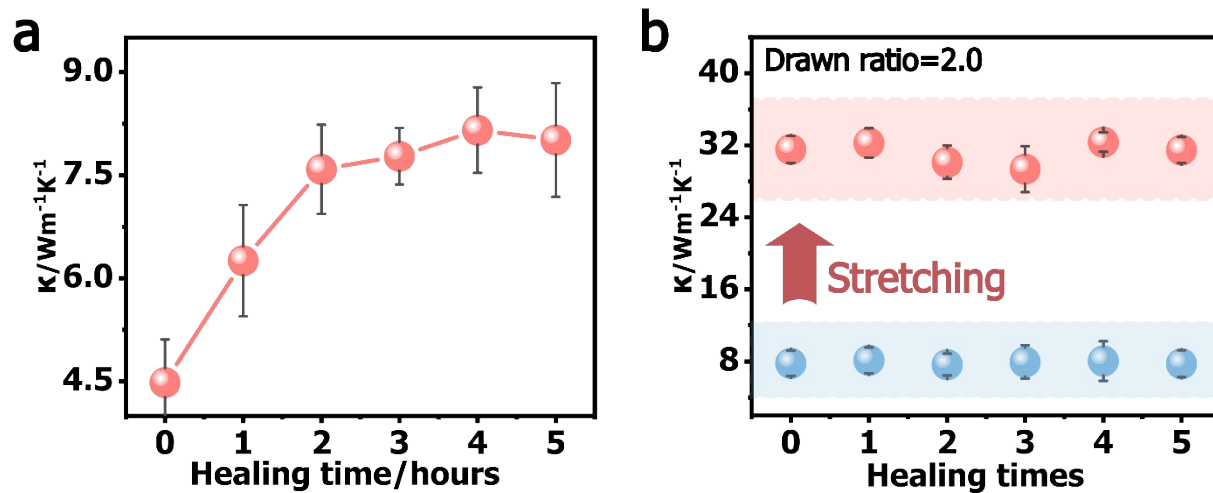
Fig. S34 a) Thermal conductivity of BNNSs$_{27}$-LM$_{27}$/PUUEC with the increase of healing time. b) Thermal conductivity of BNNSs$_{27}$-LM$_{27}$/PUUEC film after multiple times of healing (5 h), for each time, the film was further drawn with its thermal conductivity shown in red region.
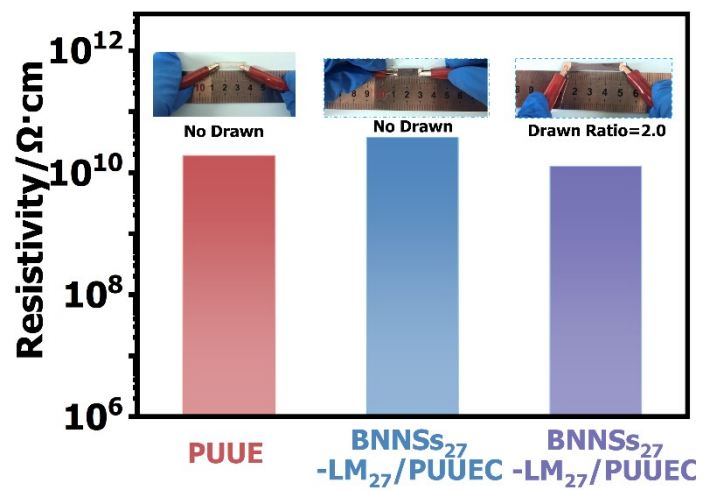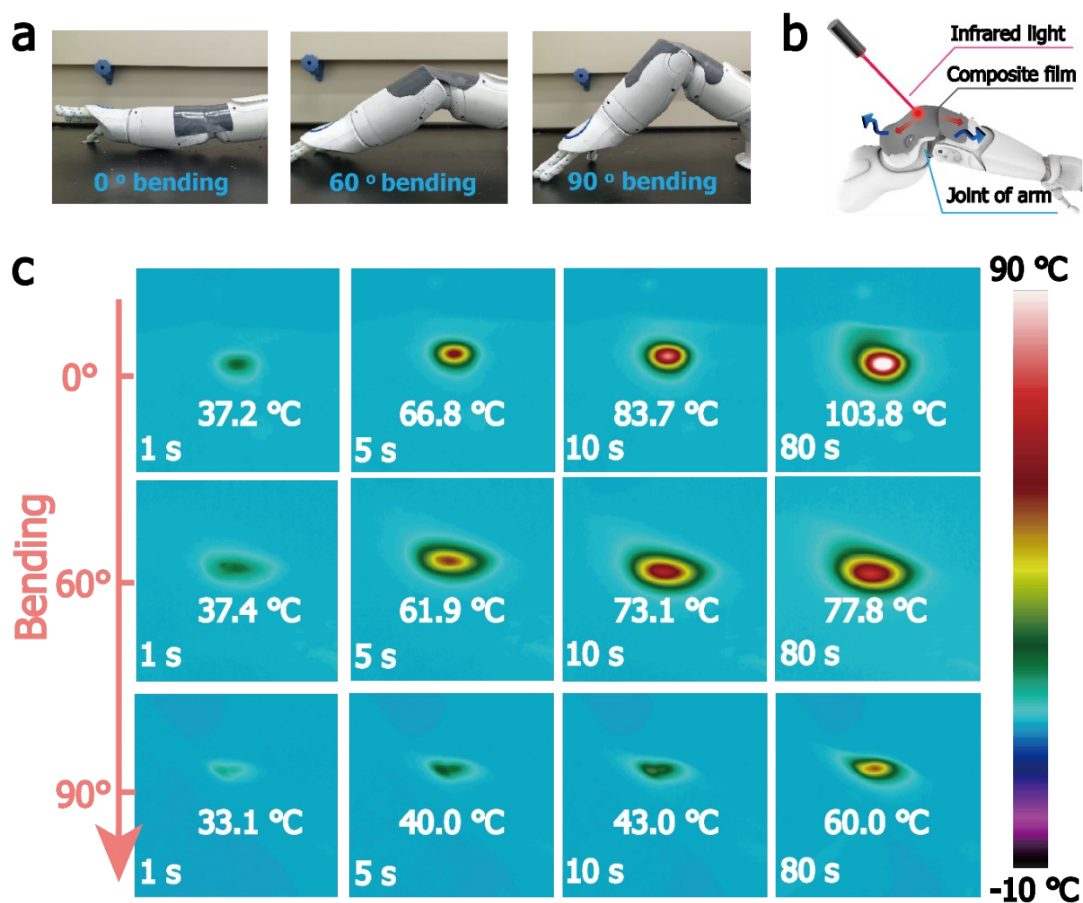
Fig. S35 Volume electrical resistivity of PUUE and BNNSs$_{27}$-LM$_{27}$/PUUEC.

Fig. S36 (a) Digital images of mechanical arms packaged by BNNSs$_{27}$-LM$_{27}$/PUUEC film with different angles of arm movement (from 0° to 90°), simulating the complex motions of a robotic machine (b) The diagram illustration for dynamic thermal management, where an infrared laser transmitter was applied to simulate the heat generated within the joint (1.5 W and the emission port is 1 cm away from the target area). (c) Infrared photos of mechanical arms during the dynamic thermal management. As depicted in Fig. S36, the platform temperature rapidly drops from 103.8 °C to 60 °C as a gradual increase of bending degree, attributed to the programmed thermal conductivity of BNNSs$_{27}$-LM$_{27}$/PUUEC, what caused by the strain-induced interfacial fusion of LM inclusions and interfacial anchored LM droplets. They could bridge adjacent BN pathways and promote efficient heat transmission upon large deformations. Therefore, these satisfactory observations in dynamic states validate the potential application of BNNSs$_{27}$-LM$_{27}$/PUUEC elastomer in robotic technology for remarkable thermal management.
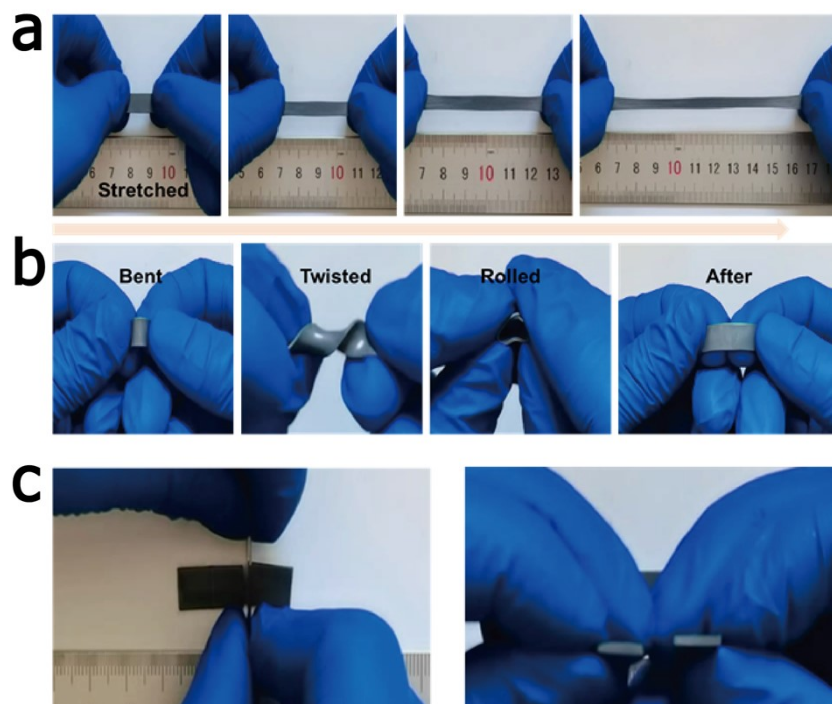
Fig. S37 a) Digital photos of BNNSs$_{27}$-LM$_{27}$/PUUEC being stretched. b) Digital photos of BNNSs$_{27}$-LM$_{27}$/PUUEC being bent, twisted, and rolled. c) Digital photos of BNNSs$_{27}$-LM$_{27}$/PUUEC being cut and its cross-sectional image. It can be clearly seen from these images that no LM leakage was observed during various operations.

References:

1   Y. Li, W. Li, A. Sun, M. Jing, X. Liu, L. Wei, K. Wu, and Q. Fu, *Mater. Horiz.* 2021, **8**, 267.

2   D. Wang, J. Xu, J. Chen, P. Hu, Y. Wang, W. Jiang, and J. Fu, *Adv. Funct. Mater.* 2020, **30**, 1907109.

3   K. Song, W. Ye, X. Gao, H. Fang, Y. Zhang, Q. Zhang, X. Li, S. Yang, H. Wei, and Y. Ding, *Mater. Horiz.* 2021, **8**, 216.

4   X. Yan, Z. Liu, Q. Zhang, J. Lopez, H. Wang, H. Wu, S. Niu, H. Yan, S. Wang, T. Lei, J. Li, D. Qi, P. Huang, J. Huang, Y. Zhang, Y. Wang, G. Li, J. Tok, X. Chen, and Z. Bao, *J. Am. Chem. Soc.* 2018, **140**, 5280.

5   Y. Wang, X. Liu, S. Li, T. Li, Y. Song, Z. Li, W. Zhang, and J. Sun, *ACS Appl. Mater. Inter.* 2017, **9**, 29120.

6   J. Kang, D. Son, G. Wang, Y. Liu, J. Lopez, Y. Kim, J. Oh, T. Katsumata, J. Mun, Y. Lee, L. Jin, J. Tok, and Z. Bao, *Adv. Mater.* 2018, **30**, 1706846.

7   F. Luo, T. Sun, T. Nakajima, T. Kurokawa, Y. Zhao, K. Sat, A. Ihsan, X. Li, H. Guo, and J. Gong, *Adv. Mater.* 2015, **27**, 2722.

8   K. Sato, T. Nakajima, T. Hisamatsu, T. Nonoyama, T. Kurokawa, and J. Gong, *Adv. Mater.* 2015, **27**, 6990.

9   A. Ihsan, T. Sun, T. Kurokawa, S. Karobi, T. Nakajima, T. Nonoyama, C. Roy, F. Luo, and J. Gong, *Macromolecules* 2016, **49**, 4245.